2.2.1 Experiment #1: Estimation of the relation between applied force and pneumatic pressure

To find the relation between the pressure variation in the circuit (due to the contact between the pneumatic balloon and an object) and the subsequent exerted force, there are two main methods: i) making a physical model of the system; ii) estimating an empirical evaluation. In a first approach to the problem we decided to discard the first option because it might be harder to accurately model the elastic deformation of the pneumatic balloon, in particular when you do not have a full characterization of the material that might significantly affect the behavior of the elastic membrane.

Thus, we conducted a preliminary experiment simulating a robot-assisted palpation task to gather data about our system and find an empirical force-pressure relation that implicitly contains the behavior of the elastic balloon. It is worth underlying that the ranges of pressure and force of interest in surgical palpation are small and this facilitates the empirical characterization and evaluation.

After demonstrating the feasibility of the pneumatic method using the experimental approach as described below, also the alternative option (i.e., modeling) has been implemented. It will be presented in Chapter 3, where the relation between exerted force and variation of pressure is the outcome of the mathematical modeling of the interaction between the pneumatic balloon and an object.

Methods During each palpation task the robotic end-effector, not in contact with the sensor initially, gradually moved towards the wall. Once it came into contact with the force sensor, an increasing force was exerted through the pneumatic balloon. Then it stopped.

We considered six different initial pressure ranges for the pneumatic balloon defined according to a pilot experiment and reported in the left column of the table in Fig. 2.5b. In this chapter, pressure values are the output of a differential sensor and thus are computed with respect to the atmospheric pressure value. The minimum pressure value was 4.0 kPa: for lower values the pressure variation would not be noticeable. The upper limit was 11.2 kPa, since for higher values the pneumatic balloon assumes a highly non-linear behaviour. In fact, for high inflating pressure values the balloon starts expanding more easily and this sudden increase of volume leads to a reduction of the internal pressure. The number of ranges (i.e., 6) was selected as the best compromise between simplicity and accuracy.

Within each range, we tested multiple values of initial pressure. In particular, starting from the first value of the range, the initial pressure was increased by 0.12 kPa each time. For each pressure value we carried out two palpation tasks in which the displacement of

the robotic end-effector was 3 mm and 6 mm, respectively. So, following this procedure we carried out 20 trials for each pressure range, ten with the end-effector displacement of 3 mm and ten with the one of 6 mm, for a total of 120 trials. The zero position was considered the one in which the elastic membrane came into contact with the sensor. This moment was detected by the sensor itself with a very small change of the measured force. The maximum robot motion was set so that the pneumatic balloon housing did not hit the ATI, preventing measurements alteration.

Results For each experimental trial, when the robotic arm stopped moving, we measured the pressure value of the proposed pneumatic system and the forces registered by the ATI sensor in the three directions of the space. Our pneumatic force sensor cannot give any information about the direction of the applied force: its single value output can be related to the norm of the three force components measured by the commercial force sensor. Although in this case it corresponds approximately to the force in the movement direction of the robotic arm, for the sake of accuracy we preferred not to ignore the minimum components in the other directions. Moreover, because of the aim of the evaluation and the way we carried out the experiment, i.e., the robotic manipulator was moving along a normal direction with respect to the sensitive surface of the sensor (y-axis in Fig. 2.3), torque components were neglected.

Fig. 2.4a shows the norm of the force measured by the ATI sensor on the top and the differential pressure measured by the Freescale MPXV5050DP on the bottom during a representative trial. At $t = 0\,\mathrm{s}$, the pneumatic balloon is completely deflated and no contact force is present ($F_i = 0\,\mathrm{N}$). At about $t = 3\,\mathrm{s}$, it reaches the initial pressure, i.e., $P_i = 5.2\,\mathrm{kPa}$ for the considered task, but there is still no contact force playing. At about $t = 8.6\,\mathrm{s}$, the balloon applies a force on the ATI sensor, that corresponds to a change of the pneumatic system pressure. The difference in terms of force ($\Delta F = F_f - F_i$, where F_f is the value of the force registered by the ATI sensor when the robotic arm stopped moving) needs to be related with $\Delta P = P_f - P_i$, where P_f is the pressure inside the pneumatic system due to the contact with the sensor.

Fig. 2.4b shows with blue stars each couple (ΔP, ΔF) collected throughout the whole experiment for the specific initial pneumatic pressure range [5.2, 6.4) kPa. The purple line represents a quadratic fitting of data obtained with a least squares method to estimate the empirical relation between ΔP and ΔF. The different equations estimated this way for any considered initial pressure range are graphically depicted in Fig. 2.5a and reported in the table of Fig. 2.5b. As expected, pneumatic balloons inflated at different initial pressure values behave differently when pressed against a surface. For the same exerted force, the variation of pressure in a more deflated balloon will be higher. The

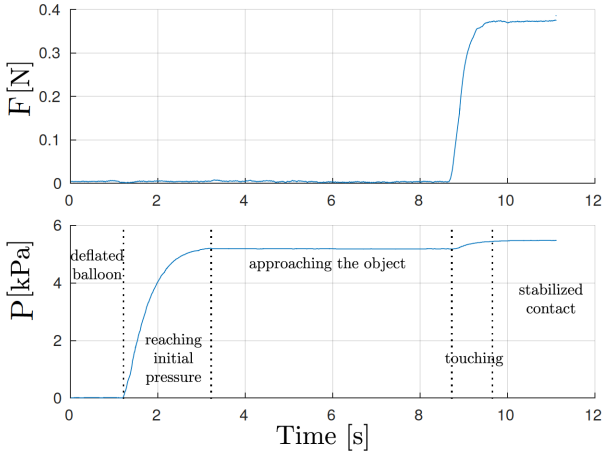

(a)

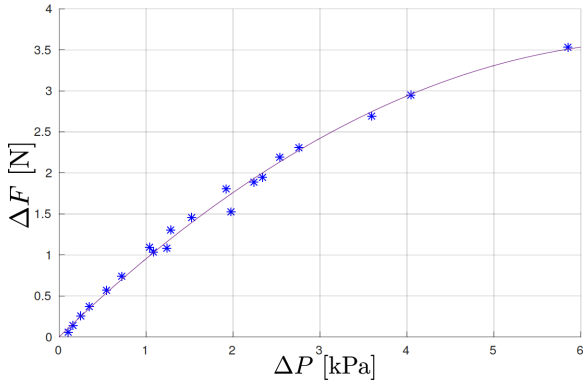

(b)

Figure 2.4: (a) The norm of the force measured by the ATI Nano 17 (upper part) and the pressure measured by Freescale MPXV5050DP (lower part). Except for the increasing pressure due to the inflating air, they have constant trends till the impact between the pneumatic balloon and the force sensor. (b) The relation between ΔP and ΔF collected throughout the whole experiment for the initial pneumatic pressure range [5.2, 6.4) kPa.

maximum reachable contact force depends on the inflating pressure value: higher contact forces cannot be reached with lower initial pressures.

Once defined the relations between the exerted force and the correspondent variation

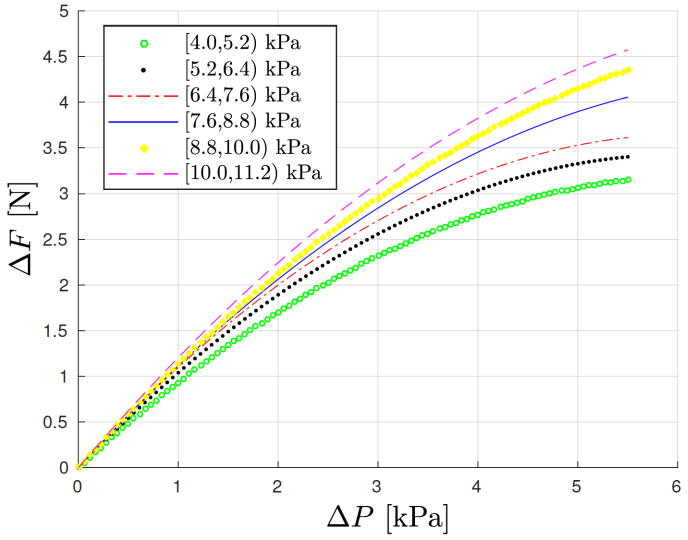

(a)

Pressure range	Relation Force-Pressure
[4.0, 5.2) kPa	$F = -0.07959x^2 + 1.011x$
[5.2, 6.4) kPa	$F = -0.09369x^2 + 1.134x$
[6.4, 7.6) kPa	$F = -0.09798x^2 + 1.196x$
[7.6, 8.8) kPa	$F = -0.0841x^2 + 1.2x$
[8.8, 10.0) kPa	$F = -0.07701x^2 + 1.215x$
[10.0, 11.2) kPa	$F = -0.08316x^2 + 1.289x$

(b)

Figure 2.5: Empirical force-pressure relations for the six considered initial pressure ranges.

of pressure, it is possible to compute the contact force in a unknown environment, from the only knowledge of the inflating pressure and the measured variation.

2.2.2 Experiment #2: Pneumatic sensor validation (making contact)

The aim of the second experiment was to validate the previously defined force-pressure relations in a single and maintained contact task, in which it was easier to compute the final estimation error since at the end of each trial the interaction force was constant.

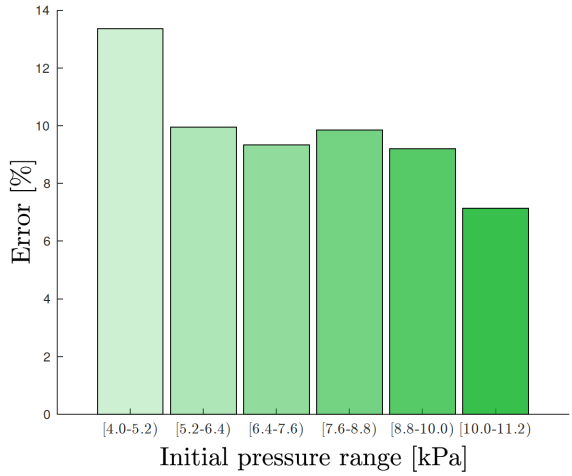

Figure 2.6: Estimation error divided among the considered initial pressure ranges comparing data retrieved by the pneumatic sensor and the ATI force sensor. Errors have been normalized over ATI sensor force values.

Methods We carried out the same procedure described in Section 2.2.1, but in this case the force measured by the ATI sensor represented only the ground truth value. Similarly to the first experiment, the task consisted in the robotic end-effector, not in contact with the sensor at the beginning, that gradually moved towards the wall and applied an increasing force on the sensor by means of the pneumatic balloon and then stopped. We carried out ten trials for each initial pressure range depicted on the left side of the table in Fig. 2.5b, for a total of 60 trials. This time, in any trial both the pressure and the displacement of the robotic end-effector were pseudo randomly picked out in the considered relative range. Regarding the displacement of the robotic end-effector, we selected the range [2,7] mm to consider a larger number of interactions with the ATI sensor. Again, the zero position was the one in which the elastic membrane came in contact with the ATI and any contact between the ATI and the pneumatic balloon housing was avoided.

Results For each experimental trial, when the robotic arm stopped moving, we measured the interaction force using both our pneumatic sensor (following the relation force-pressure detailed in Section 2.2.1) and the ATI sensor. Fig. 2.6 shows aggregated information about the error computed by the force estimation performed through the pneumatic sensor with respect to the one measured with the ATI (the ground-truth). Such

an error has been normalized over the force ground-truth value and split among the six different initial pressure ranges. The resulting mean of the normalized error is 9.81%.

We tested the means of the error normalized over the force measurements for the six considered initial pressure ranges. The collected data passed the Shapiro-Wilk normality test. To determine whether the means of the error are statistically equivalent, we performed a two one-sided t-test (TOST), whose null hypothesis (two groups are different) states that the groups must differ by at most θ to be rejected. In this work we evaluated θ as suggested in [108], where the authors provide a useful step-by-step process for performing equivalence testing with commonly available computational software packages. The tests revealed statistical equivalence for any couple of means.

2.2.3 Experiment #3: Pneumatic sensor validation (repeated making/breaking contact)

The goal of the third experiment was to validate the empirical relation described in Section 2.2.1 in a more realistic, though repeatable, palpation task. The task consisted in three different and subsequent making/breaking contact actions with the ATI sensor, followed by a stationary contact. This set of actions aims at modeling and mimicking a palpation task performed by a surgeon before the real surgical procedure.

Methods Likewise previous experiments, the robotic end-effector, not in contact with the sensor at the beginning, gradually moved towards the wall and applied an increasing force on the sensor by means of the pneumatic balloon. As soon as it reached a predetermined displacement, it started moving backward, thus decreasing the interaction force, and eventually broke the contact. Then, a similar trial started again and then again, for a total number of three subsequent making/breaking contact actions. Finally, the robot came into contact with the stationary object and stopped after moving for a certain displacement. While the initial pressure the balloon was inflated at was kept the same throughout the task, the robot displacement changed each trial: it was 5.0 mm, 5.5 mm, 6.0 mm, and 6.5 mm for the first, the second, the third, and the fourth trial, respectively. Again, the zero position was considered the one in which the elastic membrane came into contact with the ATI sensor and any contact between the sensor and the pneumatic balloon housing was avoided.

Results With respect to the previous experiment of Section 2.2.2, this test aimed at investigating the performance of the proposed sensor throughout a complete palpation task, analyzing the final steady-state interaction force as well as the transient one. During

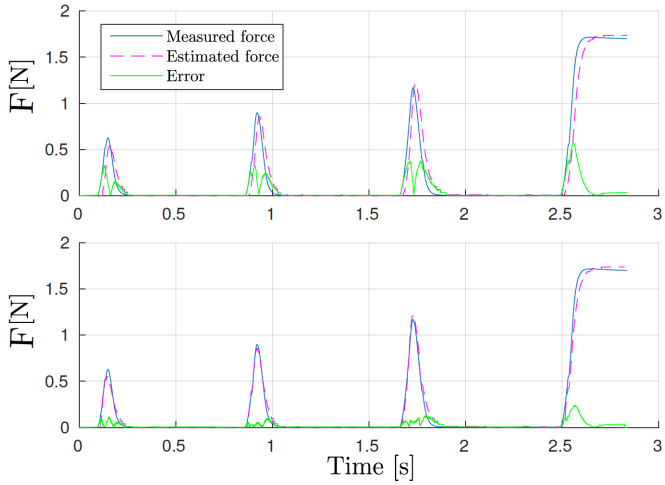

Figure 2.7: Repeated making/breaking contact actions. The solid blue line shows the interaction force measured by the ATI sensor along the y-axis (see Fig. 2.3). The dashed magenta line represents the interaction force estimated by the proposed pneumatic sensor. The dotted green line indicates the absolute error between the two aforementioned forces. On the top figure it is possible to see a delay between the developed sensor and the commercial one. On the bottom, a time shift of -0.015 s has been introduced to realign the two plots and compute a more meaningful error.

the task we measured the interaction force with the ATI force sensor, considered as ground truth, and we estimated the same force using the proposed pneumatic sensor following the proper equation characterized in Section 2.2.1.

Fig. 2.7 shows the force profiles gathered by both the ATI sensor (solid blue line) and our pneumatic sensor (dashed magenta line). During this run the initial pressure was set to 8.15 kPa. On the top, data are reported as recorded and it is worth noting the presence of a time delay between the blue and magenta force profiles due to the different dynamics of the two sensors. On the bottom, this delay has been artificially corrected introducing a constant time shift of -0.015 s to the force estimated by the pneumatic sensor.

The green dotted line represents sample by sample the absolute value of the difference between the two gathered forces and can be considered a significant metric to measure the accuracy of our sensor. For the sake of fairness, the error is shown on both the subplots. It has a maximum value of 0.5757 N when the time delay is present and 0.2417 N where it is not.

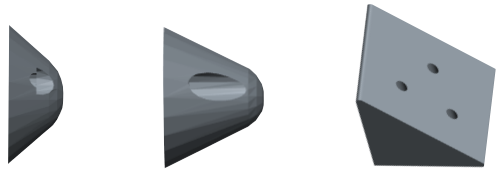

(a) (b) (c)

Figure 2.8: Three objects used to modify the profile of the contact surface (i.e., the ATI force sensor): rounded tip cones with heights (a) 8 mm and (b) 16 mm, used to obtain non-planar surfaces, and (c) a prism, used to obtain an inclined surface.

2.2.4 Experiment #4: Pneumatic sensor validation (contact with non-planar or inclined surfaces)

A possible issue in using the pneumatic sensor in real applications might be related to the contact with either non-planar or inclined surfaces. Thus, a further experiment has been carried out to evaluate how the relation between force and variation of pressure changes accordingly to the shape of the contact object.

Methods Three small objects of different shapes (shown in Fig. 2.8) were designed and firmly attached one at a time to the ATI sensor. Two were rounded tip cones with the same base area but different heights (8 and 16 mm), and, thus, different slopes (see Fig. 2.8a and Fig. 2.8b). One was a prism mounted so that the contact surface with the robotic end-effector was inclined with respect to the direction of motion (see Fig. 2.8c). The robotic end-effector moved towards the wall and stopped after coming into contact with the object attached to the ATI sensor.

We carried out ten trials for each object. In each trial the pressure and the displacement of the robotic end-effector were pseudo randomly picked out in the ranges [10, 11.2) kPa and [2, 7] mm, respectively. The zero position was the one in which the elastic membrane came in contact with the object attached to the ATI. Again, any contact between the object and the pneumatic balloon housing was avoided.

Results For each experimental trial, when the robotic arm stopped moving, we used the ATI sensor to measure the interaction force between the balloon and the object attached

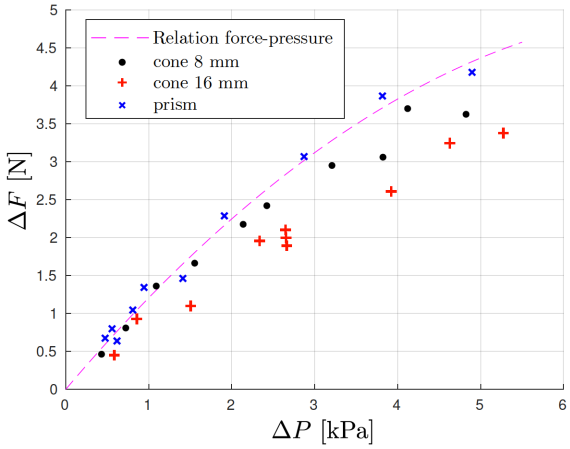

Figure 2.9: Comparison between the force-pressure relation identified in Section 2.2.1 for the pressure range [10, 11.2) kPa (dashed magenta line) and the experimental data collected using three different surfaces.

to the ATI (ΔF), and we measured also the variation of pressure inside the balloon (ΔP). Fig. 2.9 shows the couples (ΔP, ΔF) collected in the whole experiment and compared to the previously identified force-pressure relation for the range [10, 11.2) kPa.

The results obtained using the cones depicted in Fig. 2.8a (8 mm high) and Fig. 2.8b (16 mm high) may suggest that the actual force-pressure relation depends on the shape of the contact surface and does not correspond to the previously identified relation. For the same variation of pressure, the force measured by the ATI sensor (black dots and red crosses) is lower than the estimation that would be performed by the pneumatic sensor (dashed magenta line). This difference increases with the slope of the cone. On the contrary, when the pneumatic balloon is pressed against a flat and inclined surface (the prism of Fig. 2.8c), the results are comparable to the ones obtained in the previous experiments. In this case, despite the balloon is not homogeneously pressed, the estimation of the pneumatic sensor corresponds to the force measured by the ATI.

2.3 Discussion

By performing different experiments, both the steady-state and the transient behavior of the pneumatic sensor have been evaluated. Moreover, the pneumatic balloon has been tested with different contact surfaces. Although the aggregated results depicted in Fig. 2.6

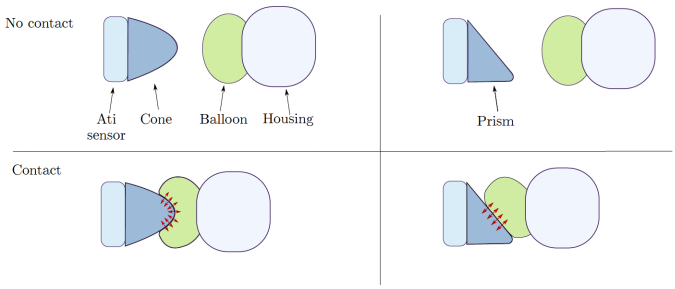

Figure 2.10: A schematic representation of the contact between the balloon and (left) a rounded tip cone, (right) a prism. Top view is used to simplify the representation.

were declared statistically equivalent, it is worth noting that the pneumatic sensor appears less accurate with a lower initial pressure. This might be due to the fact that the absolute error value is comparable among the different pressure ranges but measured forces at low initial pressure are lower and thus a small absolute error might result in a higher error ratio. This trend is also confirmed for the highest pressure range, in which the error ratio is the lowest.

Even though Fig. 2.7 shows a slightly slower dynamics of the proposed pneumatic system with respect to a high-bandwidth very-fine resolution commercial sensor (constant time delay of 0.015 s), the two force profiles result almost overlapped no matter the continuous change of interaction forces. This proves a high reliability of the system both in the transient and in the steady-state interaction. However, the nature of this delay will be further investigated in future works together with its relation to the pneumatic system hoses length and diameter.

The fourth experiment did not aim at computing the error between the force measured by the ATI sensor and the one estimated by our pneumatic device, but it focused on qualitatively investigating whether the force-pressure relations identified in Section 2.2.1 may change depending on the shape of the contact surface. From the results of this experiment we may argue that force values measured by the ATI do not lie on the previously identified curve, thus are different from those expected, only when the pneumatic balloon is subject to indentation, which is caused by the contact with an object with a small edge with respect to the balloon surface (i.e. cones). Indeed, both using cones and prism the membrane is not homogeneously pressed, but in the latter case this does not influence the relation between force and variation of pressure. To be more specific, we suppose that, in case of indentation, part of the contact force between the balloon and the cone can

not be properly measured by the ATI sensor, because of symmetric components that are compensated (see the red arrows in the left part of Fig. 2.10). However, these components affect the pneumatic balloon internal pressure value, and thus they are measured by the pneumatic sensor. As shown in Fig. 2.9, the missing component of force measured by the ATI is proportional to the slope of the cone.

The preliminary results obtained with the prism indicate that the aforementioned behavior is related only to the indentation of the membrane and not to the inclination of the contact surface. Indeed, when the membrane is unevenly deformed by the contact surface but there is no indentation (i.e., the case shown in the right part of Fig. 2.10), the exerted force may have components which are not along the movement direction of the robotic arm, but each component influences both the value of pressure inside the balloon and the measurement carried out by the ATI sensor. Thus, using the prism, despite the balloon is not homogeneously pressed and the force has significant values in each of the three components, the estimated norm of the force is comparable to the values already collected for planar surfaces normal to the movement direction.

In the end, limitations of the pneumatic sensor in case of contact with particular shapes were not actually demonstrated. When the considered surface causes indentation it is simply not possible to prove the correctness of force estimation through the comparison with the ATI sensor. In fact, the pneumatic force measurement takes into account also the components which are symmetric with respect to the indentation, which can not be measured by the ATI. However, they would be actually perceived by user's fingertip during palpation in open surgery, thus it is important to include them in the final force value. It is also important to consider that in robotic surgery applications (e.g., abdominal or thoracic procedures) it is highly improbable to encounter surfaces which can not be considered approximately planar, since involved surfaces are tissues and organs of the human body. In addition, we assume that by reducing the sensor size the contact surface will result locally planar with respect to the pneumatic balloon.

Our results have been compared to the work Faragasso et al. published in 2014 [69], in which a system combining vision and a spring mechanism to measure interaction forces in MIS was developed. They proposed two different models, a mathematical and an experimental one, with a RMSE of 0.1535 N and 0.1355 N, respectively, in the range [0, 1.96] N. Computing the RMSE only on the data in the same force range that we collected during the validation experiment of Section 2.2.2, we found a value of 0.1121 N, comparable, if not lower, to the ones calculated by Faragasso et al.. The work of Faragasso et al. has been chosen for a comparison because the experimental approach they exploited is similar to the one developed in this thesis. Other similarities are the non-invasive and small size device and the possibility of modifying the measurement

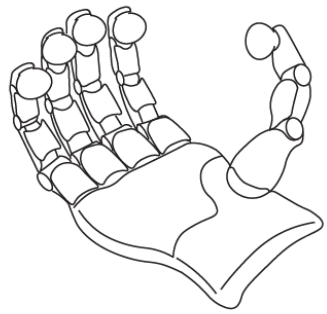

Figure 2.11: Sketch of a robotic hand equipped with pneumatic balloons.

range and the sensor stiffness (changing the spring constant in one case, and setting the initial pressure in the other). However, besides calculating the force with a lower error in the same range, the pneumatic device measures higher forces up to 4.5 N with reasonable errors. Moreover, the major advantage of our system with respect to the aforementioned one is the possibility of changing online the measurement range and the compliance of the sensing part according to the tissue to touch, while in [69] these features strictly depend on the structure of the device and the stiffness of the spring used.

A pneumatic force sensor as the one here proposed gives the user the possibility of deciding the initial pressure according to needs, and thus to obtain a sensor with adjustable compliance and range of forces. High-pressure (and thus high stiffness) balloons can be more suitable for rigid tissues, where we expect to exert higher forces. For softer tissues it would be better to inflate the membrane at a lower pressure, so as to achieve a less invasive palpation and measure contact forces without damaging them.

2.3.1 Further applications

Besides the application in RMIS that represents the main goal, the proposed system might be used also for different purposes. For instance a set of these pneumatic sensors can also be seen as the fingerpads of a robotic hand/gripper, whose compliance of the grasp can be real-time tuned. During remote manipulation tasks, a robotic hand equipped with pneumatic force sensors as the one proposed in Fig. 2.11 may take advantage of the strengths of both soft and rigid robotic approaches. It would be capable of precise and fine grasps, eventually becoming a completely rigid hand when all the balloons are

hidden deflated into their housings. In case of fragile objects to be grasped, balloons can be inflated to modify the stiffness of the hand and, thus, achieve a safer grasp. In addition, the pneumatic sensors would be used anytime force measurements are needed. Additional force sensors would not be required anymore to measure the interaction forces between a robotic hand (or gripper) and an object, because the sensing system would be integrated into the hand itself. Different designs may be studied in according to different applications, without changing the whole rigid structure of the robotic hand/gripper. For example, considering a hand, multiple balloons can be placed in each finger or in the palm to enable force measurement at each contact point. Besides this, different patterns of balloons, whose stiffness can be independently adjusted, may help in tuning the softness of the interaction.

2.4 Conclusions

This chapter introduces the design of a novel pneumatic force sensor for robot-assisted surgery, that takes advantage of the measurement of a pressure change inside an elastic membrane to estimate the interaction force between the surgical tool and the patient's tissue. The balloon can be inflated only when required, without constraining the surgeon's workspace during the standard medical procedures. Moreover, the delocalization of the electronics with respect to the elastic membrane makes this surgical tool inexpensive and easily disposable because of sterilizability reasons.

Firstly, to characterize the usability of the proposed sensing system, we empirically evaluated the relation between the variation of the pressure inside the elastic membrane and the applied force, considering six different ranges of the initial pneumatic pressure. Then, we validated the computed functions exploiting a commercial F/T sensor as ground-truth twofolds: i) during a single and maintained contact; ii) during four subsequent interactions with an object that mimic a complete palpation task. The sensor behavior has been also investigated in case of contact with non-planar and inclined surfaces.

The force-pressure relations shown in Fig. 2.5 strictly depend on the elastic membrane material and on the system size so, with a view to future applications, the system needs to be calibrated when any main component changes. This limitation has been overcome in Chapter 3, where a mathematical model of the pneumatic sensor behavior is proposed.

The use of a gas as a means to estimate interaction forces allows one to change the initial balloon pressure, thus the stiffness of the tool, according to the tissue to be touched and the amount of force to exert. It is clear how the same pressure change leads to different interactions forces, when the initial pneumatic pressure varies. Indeed, the maximum force the pneumatic sensor can estimate is limited by the inflating pressure

value, but it can be quickly changed during palpation itself, providing as input to the system a different value of pressure in according to the required stiffness of the balloon.

In this work, the pneumatic balloon has been made in latex. Rubber latex has a higher elastic behavior than other materials, and extraordinary and natural hypoallergenic and antibacterial properties. However, the concept of biocompatibility is not absolute: latex is considered biocompatible and is a standardized material for medical applications, but it could happen that some people have allergic reactions. In this case, it can be easily replaced by different materials, which will not change the working principle of the device. The gas used to inflate the inflatable balloon can be air, but any biologically compatible gas can be used if required.

Despite the simple and intuitive technology exploited to design the proposed pneumatic system, the presented preliminary results appear very promising and we believe that this working principle represents a valuable contribution for the development of inexpensive sensors to be used in RMIS scenarios. Due to the simple mechanical miniaturizable structure, the prototype described in this work will be able to meet the size limitations for robotic surgery.

Chapter 3

A mathematical model of the pneumatic force sensor

This chapter extends the proof of concept presented in Chapter 2, further developing a pneumatic force sensor taking advantage of an air-filled balloon. The goal of Chapter 2 was to introduce a new pneumatic-based method to measure, or at least estimate, interaction forces between robotic surgical tools and tissues/organs of the human body. It relies on the relation between exerted force and variation of pressure inside a tiny pneumatic balloon, used as remote fingerpad to palpate the tissues of interest. Here, we pursued the same idea by proposing a more general mathematical model.

The pneumatic balloon was modeled as a spherical elastic membrane, whose behavior during contact was characterized taking into account both the deformation of the membrane and the compression of the contained gas. Geometrical considerations combined with an energetic approach allowed us to compute the force of interest. The effectiveness of the sensing method has been confirmed by experimental results, based on comparison with the same high-performance commercial force sensor already exploited in the experimental validation of Chapter 2.

3.1 A mathematical model

Based on the previous achievements, this work aims at investigating and defining the relation between the contact force and the variation of internal pressure inside the pneumatic balloon. The main outcome of Chapter 2 was that the norm of the contact force and the resultant increase of the pressure inside the balloon were related through a quadratic function experimentally detected. The coefficients within this relation depended on the value of the pressure the balloon had been inflated to. Even though the experimental relation identified in Chapter 2 was suitable to estimate the contact force, we believe that a mathematical model is necessary for further development of our sensor. Thanks to a model characterizing the sensor's behavior, calibration is not needed anymore each time

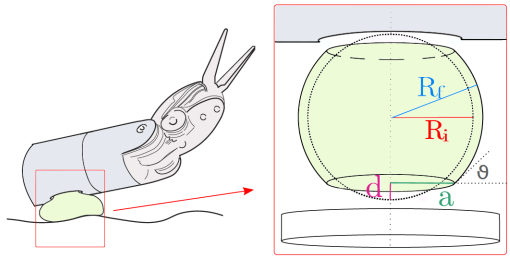

Figure 3.1: Working principle and sketch of the pneumatic sensor: undeformed (dashed) and deformed (green) states of the membrane.

size or material of any components of the pneumatic circuit change.

To derive the mathematical model we assumed that:

- ◇ the considered pressure range allows us to treat the behavior of the membrane using linear elasticity theory, since deformations are reversible and relatively small;
- ◇ the shape of the inflated balloon is a sphere, whose radius is known for each value of inflating pressure;
- ◇ the tissue of interest is always stiffer than the sensor and is considered to be flat (with a radius of curvature much bigger than the radius of the balloon).

The contact between the pneumatic balloon and the human tissue was modeled as the one between a deformable, homogeneous, elastomeric, spherical membrane and a solid. Fig. 3.1 shows the membrane before and after the contact.

The balloon is initially inflated with a certain overpressure of gas ΔP_i, which is the difference between the internal pressure P_i and the atmospheric pressure P_0.[1] Therefore, it is characterized by a radius R_i and a membrane thickness h, both proportional to ΔP_i. After the contact, due to the compression of the internal gas and the elasticity of the membrane, the pneumatic balloon adopts the shape of a sphere characterized by a wider radius $R_f > R_i$, with two flattened areas. We supposed these two contact surfaces are equivalent. The pneumatic balloon balances the increased pressure P_f by stretching, increasing surface area, and diminishing h.

[1] In the previous chapter, for simplicity of notation, P was the differential pressure value measured with respect to the atmospheric pressure, while ΔP was the pressure variation due to the contact. Here we need to distinguish absolute and differential pressure values inside the balloon, thus the notation is slightly different. In this case, P is the absolute value of pressure, while $\Delta P = P - P_0$ is the differential value. The pressure variation due to the contact is $P_f - P_i$.

Since the internal pressure is equally distributed in the whole circuit, the contact force we aim to compute is

$$F = \Delta P_f \pi a^2 \tag{3.1}$$

with a the radius of the circular contact surface and ΔP_f the difference between P_f and P_0. Defining as d the deformation due to the contact as depicted in Fig. 3.1, the contact radius a is

$$a = \sqrt{{R_f}^2 - (R_i - d)^2} \tag{3.2}$$

Since ΔP_f is measured, the only unknowns are d and R_f.

3.1.1 State of the art in modeling deformation of spheres

Before describing the developed mathematical model, a brief overview of the state of the art in modeling deformations of spherical solids is presented. For example, Lulevitch et al. [109] evaluated the contact force leading to deformation of microcapsules using an energetic method and the assumption of constant volume before and after the contact, which is reasonable only for small deformations. The total reaction force proposed in their paper has two components (stretching and bending) and reads:

$$F = F_{str} + F_{bend} = \frac{2\pi E h d^3}{(1-v){R_i}^2} + \frac{\pi}{\sqrt{2}} E h^2 \sqrt{\frac{d}{R_i}} \tag{3.3}$$

where E is Young's modulus and v is Poisson's coefficient of the membrane. In our application, for deformations leading to a small reduction of the volume, we might neglect the compression of the balloon (and thus the variation of volume) and assume to be in the same conditions described by Lulevitch et al. in [109]. In this case, an approach to compute the force of interest may consist in equalizing Eq. (3.3) to Eq. (3.1), considering also Eq. (3.2):

$$\Delta P_f \pi [{R_f}^2 - (R_i - d)^2] = \frac{2\pi E h d^3}{(1-v){R_i}^2} + \frac{\pi}{\sqrt{2}} E h^2 \sqrt{\frac{d}{R_i}} \tag{3.4}$$

The two unknowns in this equation are d and R_f, but, from volume conservation [109], R_f could be approximated to

$$R_f = R_i + \frac{d^2}{2R_i} \tag{3.5}$$

Thus, substituting Eq. (3.5) in Eq. (3.4) it is possible to easily compute d and, then, the exerted force from Eq. (3.1).

Shanahan [110] proposed another formula to compute the difference between R_f and R_i, knowing P_f and P_i:

$$\Delta R = \frac{R_i^2(1-v)(P_f - P_i)}{2Eh - R_i(1-v)(P_f - P_i)} \tag{3.6}$$

Also his work is limited to small deformations, but it is not based on volume conservation. Thus, another option to estimate the contact force is to use Eq. (3.6) in the computation of the contact radius a and then equalize the contact force in Eq. (3.1) and Eq. (3.3) (i.e., using Eq. (3.6) in Eq. (3.4)). Since not even Eq. (3.3) has been obtained from simplifications based on volume conservation, here the computation takes into account the variation of the volume of the balloon.

Both these reasonings are effective, but for larger deformations the assumptions at their roots are no longer valid. For this reason, we studied a new mathematical method: the approach proposed in this thesis is based on the elasticity theory combined with the evaluation of the compression of the gas, thus it takes into account also the variation of volume due to the contact.

3.1.2 Energetic approach

The contact force we aim to estimate both deforms the membrane and compresses the gas contained within it. Thus, the contributions influencing the force are the stretching and the bending of the membrane, together with the compression force.

3.1.2.1 Stretching

The stretching energy is

$$E_{str} = \frac{h}{2} \int \sigma\epsilon \, dS$$

where ϵ is the two-dimensional strain tensor, σ is the two-dimensional stress tensor, and the integration is over the balloon's surface.

The thickness h of an inflated balloon depends on its radius. Since the volume of the membrane itself ($4\pi R^2 h$) remains essentially constant [110], the thickness is

$$h = h_0 \frac{{R_0}^2}{{R_i}^2}$$

where R_0 and h_0 are the radius and the thickness of the deflated membrane, respectively. We supposed that h remains constant during the compression. Being an isotropic spherical

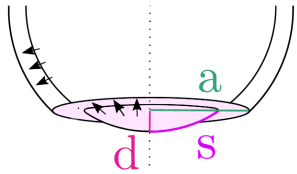

Figure 3.2: Sketch of membrane while stretching. The pink area indicates the contribution of the spherical cap in low pressure cases.

membrane, the relation between stress and strain tensors is

$$\sigma = \frac{E\epsilon}{(1-v)}$$

To finally estimate the stretching energy, we made two different evaluations depending on the extent of deformation the membrane is subjected to.

For small deformations, from the assumption that the deformed balloon has a spherical shape as well, the strain is

$$\epsilon = \frac{R_f - R_i}{R_i} \tag{3.7}$$

and thus the stretching energy corresponds to

$$E_{str} \approx \frac{4Eh\pi}{(1-v)}(R_f - R_i)^2 \tag{3.8}$$

In this case, to compute the stretching energy we used a similar approach to the one discussed by Lulevich et al. in [109].

Instead, to compute the stretching energy for larger deformations, we assumed that it was reasonable to split the two contributions of *i*) the spherical caps and *ii*) the remaining surface of the sphere, as depicted in pink and white, respectively, in Fig. 3.2. We supposed that the two spherical caps stretch to become the two flat contact areas (highlighted in pink). Defining as s half the length of the cap's arc, the strain is

$$\epsilon = \frac{a - s}{s}$$

To simplify the computation, s can be approximated to the chord $\sqrt{2R_i\, d}$. Apart from the spherical caps, the balloon's surface stretches increasing the radius of the sphere (see Eq. (3.7)). The resulting stretching energy is

$$E_{str} \approx \frac{4Eh\pi}{(1-v)}\left[\left(\frac{R_f - R_i}{R_i}\right)^2 (R_i^2 - R_i d) + \left(\frac{a-s}{s}\right)^2 (R_i d)\right] \tag{3.9}$$

To distinguish between small and large deformations, we analyzed the initial inflating pressure value. At the same exerted force, higher pressure balloons are subject to a smaller deformation, and thereby a smaller contact area. Thus, if the inflating pressure value is higher than a certain threshold, we can assume that the balloon maintains a spherical shape. If it is smaller than the threshold, the contribution of the final flat surfaces to the stretching energy is not negligible anymore. In this case, the large contact areas are supposed to be given from the stretching of the spherical caps.

3.1.2.2 Bending

Once computed the stretching energy, we considered the bending. The contribution of the bending to the whole elastic energy is negligible for a thin membrane, except near the edge of the contact area. An estimation of the bending energy can be made treating the membrane locally using beam theory [111]. Then, the elastic energy of bending is

$$E_{bend} = \frac{E\,I}{2}\,\frac{h\,L}{\rho^2} \tag{3.10}$$

where $I = h^3/12$ is the second moment of area of "beam" cross-section, $L = 2\pi\,a$ is the length of the contact circle, and ρ is the local radius of curvature, of order h/θ, with θ the contact angle. Manipulating Eq. (3.10) and approximating $\theta \approx sin\theta = a/R_f$, the bending energy is

$$E_{bend} = \frac{E\,h^2\,\pi}{12}\,\frac{a^3}{{R_f}^2}$$

3.1.2.3 Compression of the gas

Together with the elastic energy of the membrane, we considered also the work related to the compression of the internal gas. Since it is assumed to be an ideal gas, the increase in free energy due to compression is

$$\begin{aligned} E_{compr} &= -\int_{V_i}^{V_f} \Delta P\; dV = -\int_{V_i}^{V_f} \left(\frac{P_i\,V_i}{V} - P_0\right) dV \\ &= -P_i\,V_i\,\ln\frac{V_f}{V_i} + P_0\,(V_f - V_i) \end{aligned} \tag{3.11}$$

with V_i and V_f the volume of the whole circuit before and after the contact, respectively. V_i is given by the sum of the volume of all the pipes, defined as V_c, and the volume of the sphere of radius R_i, defined as V_{si}. The balloon after the contact is modeled as a sphere of radius R_f (thus, volume V_{sf}), without two symmetrical spherical caps. Thus,

the volume of the whole circuit after the contact is

$$V_{\mathrm{f}} = V_c + V_{sf} - 2\pi H^2(R_f - H/3)$$

where $H = d + \Delta R$ is the height of the spherical cap. Since pressure variation involves the whole pneumatic circuit, the contact geometry can not be described by looking only at a close neighborhood of the contact surface: the behavior due to the presence of the whole circuit should be taken into account. However, V_c is a constant value and it should be computed once for every identical systems.

3.1.3 Contact force

The total reaction force, applying Castigliano's theorem, is

$$F = \frac{\partial}{\partial(2d)}\left(E_{str} + E_{bend} + E_{compr}\right) \tag{3.12}$$

where the unknowns are the deformation d and the new incremented radius R_f. To find a relation between these two unknowns, the ideal gas law can be used to write an equation in which the only unknowns are again R_f and d:

$$V_c + V_{si} = \frac{P_f}{P_i}[V_c + V_{sf} - 2\pi H^2(R_f - \frac{H}{3})] \tag{3.13}$$

Once R_f has been written as a function of d using Eq. (3.13), we can equalize Eq. (3.12) to Eq. (3.1) to obtain an equation where d is the only unknown. Solving this equation, we can compute the contact radius a from Eq. (3.2) and finally the reaction force from Eq. (3.1).

It is worth pointing out that, in case of small deformations, the main difference between our approach and the one exploited by Lulevich et al. is that the final radius R_{f} is computed from Eq. (3.13), taking into account volume variation.

3.2 Model validation

3.2.1 System description

We herein report a brief description of the system we used to validate our method. The balloon we chose was a latex membrane 0.2 mm thick, embedded in a 3D-printed housing made of ABSPlus (Stratasys Inc., USA), including an opening to let the sensor come out.

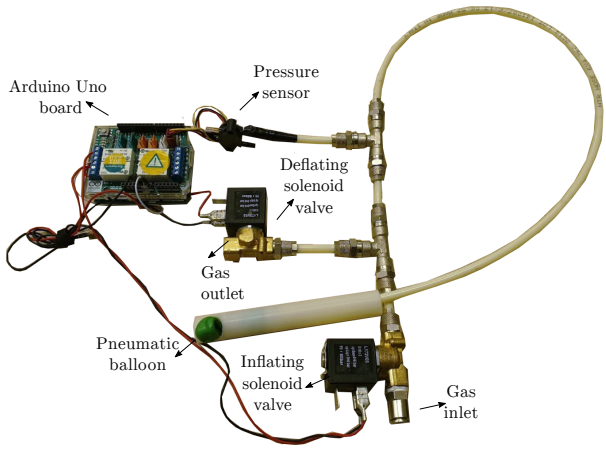

Figure 3.3: Pneumatic circuit exploited in the experimental validation.

Natural rubber latex typically has a Poisson's coefficients of 0.5 meaning the membrane keeps a constant volume while being deformed, and a Young's modulus of 2 MPa [112]. The pneumatic circuit was composed of an air compressor Ciao 25/185 (FNA S.p.A., IT), two solenoid valves L172 2/2 G1/8 (Asco Numatics Sirai S.r.l., IT), a differential pressure sensor MPXV5050DP (Freescale Semiconductor, USA), an Arduino UNO board combined with a 4 Relays Shield (Arduino, IT), and some pipes and airtight fittings to connect the different components. The volume of all the pipes V_c was $12.68 \times 10^3 \text{mm}^3$.

To avoid blast air waves during the inflating phase, undesired pressure variations, and sensor noise, the tank air compressor was equipped with a pressure regulator, the couplings were leakproof, and pressure sensor readings were processed through a first order exponential filter. After giving the desired pressure value as input to the system, the air flow was controlled by two solenoid valves. The electronic board managed their opening to inflate, deflate or lock the circuit when reached one of the two thresholds, corresponding to the preset pressure value $\pm$ the hysteresis of 0.1 kPa. The latter was introduced to prevent malfunction due to oscillations of the internal pressure when close to the chosen value.

In Fig. 3.3 the pneumatic circuit is shown. For the scope of this work, a simple prototype of the tool has been used. With respect to the setup exploited in Chapter 2, the size of the circuit has been partially reduced.

To validate our method we conducted an experimental evaluation, comparing the

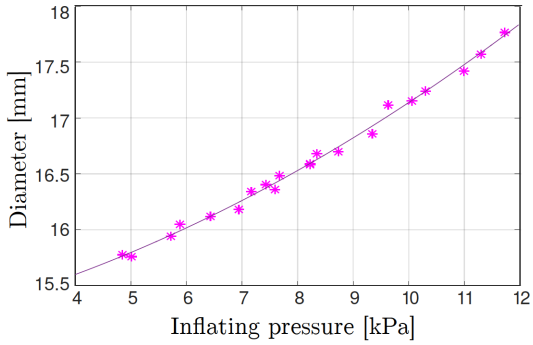

Figure 3.4: Empirical relationship between the diameter of the balloon and the inflating pressure.

estimation of the force performed by our sensor with the measures of a high resolution commercial one, the ATI Nano17 six-axis F/T sensor (ATI Industrial Automation, USA), considered as ground truth. We implemented the algorithm in MATLAB 2015b (MathWorks Inc., USA).

3.2.2 Experimental evaluation

First, the relationship between the inflating pressure ΔP_i and the radius of the inflated balloon R_i had to be found. Thus, we carried out a preliminary experiment measuring the balloon diameter in 22 trials at different inflating pressures. To accurately measure its value, we used a high-precision caliber (0.01 mm resolution) and a magnifying glass ensuring that the contact was not affecting measurements. Then, data were interpolated to find the relation between the initial radius and the inflating pressure, which was $R_i = (5.9695\,\Delta P_i^{\,2} + 44.652\,\Delta P_i) \times 10^{-3} + 7.503$. In Fig. 3.4 the quadratic fitting is shown. The radius of the deflated membrane R_0 was 7.503 mm. Then, two experiments were conducted to validate the method explored in Section 3.1.

3.2.2.1 Peak force estimation

First, the proposed method was validated through a comparison between the force estimated by the pneumatic sensor and the value measured by the ATI during the steady-state interaction.

Methods We performed 27 trials testing different values of inflating pressure ΔP_i, limiting the possible range to [4.95–11.45] kPa. For lower values, the membrane is so

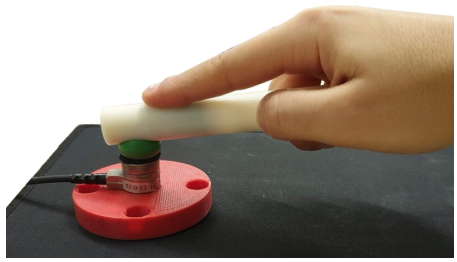

Figure 3.5: Experimental procedure: the pneumatic sensor is manually pushed toward the ATI F/T sensor, considered as ground truth.

deflated that its shape under deformation can not be approximated to a sphere and its behavior is considered to be unpredictable. On the other hand, for higher values than 12 kPa, it starts expanding more easily, increasing quickly its volume and leading to a reduction of the internal pressure.

The same procedure was repeated for each trial. At the beginning, the operator set the desired pressure value to be provided to the system. Starting from the first value of the range, the initial pressure was increased by 0.25 kPa in each trial. For each inflating pressure value, 12 subsequent making/breaking contact actions with the ATI sensor were carried out, for a total of 324 interactions. Differently from the experimental validation carried out in Chapter 2, in which a robotic arm was used, here the pneumatic balloon in its housing was manually pushed toward the ATI, which in turn was rigidly attached to a flat surface (see Fig. 3.5). During palpation in real surgical procedures the orientation of the sensing system will not be constrained to be always perpendicular to the anatomical surface. For this reason, we preferred to carry out manually the experimental validation, taking into account all the uncertainties due to the surgeon's behavior.

For each trial we obtained a force profile as the ones depicted as examples at the bottom of Figs. 3.6, which represents the norm of the force measured by the ATI. Although the norm corresponds approximately to the force in the normal direction, for the sake of accuracy we preferred not to ignore the minimum components generated by the user's movement in the other directions. The friction torque components at the contact site were negligible. As well as the pressure, the measurements collected by the ATI were processed through a first order exponential filter.

At the top of Figs. 3.6 the data gathered by the differential pressure sensor are depicted. For each contact action we identified ΔP_i as the minimum value before the pressure peak (yellow star), ΔP_f as the maximum (red star), and the ground truth as the ATI force peak.

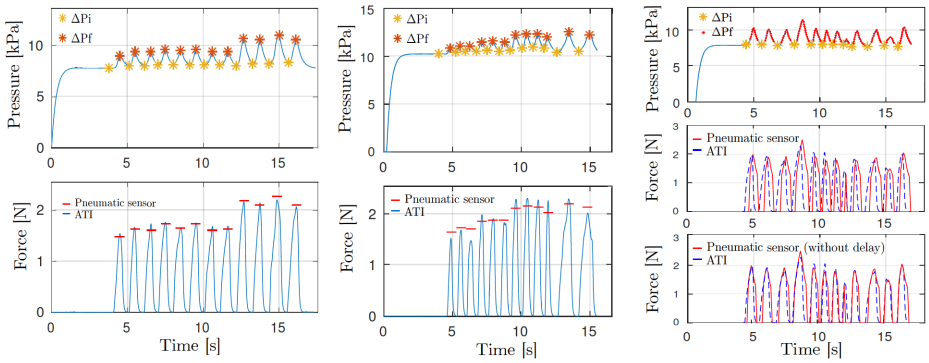

Figure 3.6: On the top, the pressure measured by the sensor Freescale MPXV5050DP. The yellow stars represent the ΔP_{i} values, while the red stars are the peak values reached after contact ΔP_{f}. On the bottom, the norm of the force measured by the ATI. The first two figures are representative trials where contact actions were executed at (a) low speed, (b) higher speed. For each contact action, the red dashes indicate the peak force values estimated by our sensor. (c) Representative trial where the contact force was estimated also during the transient. For each contact action we obtained a whole force profile.

Because of the aim of the evaluation, i.e., to validate the system in the most uncertain environment, the time elapsed between two subsequent contact actions has been chosen randomly. When faster movements were executed, after breaking contact, the pressure inside the balloon started decreasing without reaching the initial inflating value, since a new contact occurred in the meanwhile. Thus, for the sake of accuracy we did not approximate the new ΔP_i as the initial inflating value, but it was measured for each contact, and the correspondent R_i was computed again.

In the stretching energy computation, to distinguish the two cases requiring the use of either Eq. (3.8) or Eq. (3.9) (small and larger deformations, respectively) we used as threshold the pressure value of 8.85 kPa, which identifies the last two fifths of the range. For higher inflating pressures, the variation of volume with respect to the initial sphere is very small. This value, computed as

$$\frac{\Delta V}{V_{si}} = (1 - \frac{P_i}{P_f})\frac{V_i}{V_{si}}$$

ranges from 0.01 to 0.18 (mean 0.095) for ΔP_i >8.85 kPa, while it reaches twice that

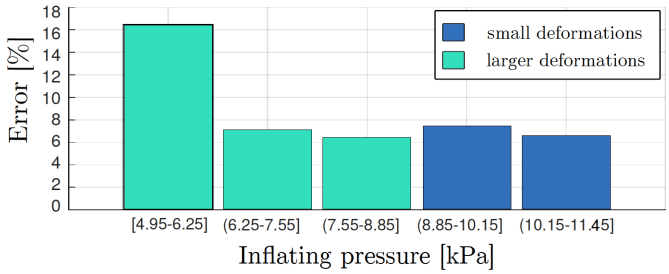

Figure 3.7: Mean percentage errors in terms of pressure. Two colors have been used to indicate different procedures for the stretching energy computation.

amount for lower pressures.

Results The red dashes in Figs. 3.6a and 3.6b represent the estimated peak force for each contact action. While the results in Fig. 3.6a were obtained moving slowly the sensor, in Fig. 3.6b a case where R_i changes time to time is shown. Also in this second condition, our system achieved promising results. The mean errors normalized over the force ground truth are 2.88% in the first case (Fig. 3.6a) and 6.19% in the second one (Fig. 3.6b). Considering the whole experiment, the mean error is 9.14%. We excluded from the evaluation those trials in which the contact did not result in an appreciable variation of pressure ($P_f - P_i$ <0.5 kPa).

In Fig. 3.7 the mean percentage errors divided among five pressure subsets are depicted. The last two columns have been colored in blue to highlight they have been obtained following a different procedure for the stretching energy computation. The accuracy of our estimations clearly decreases at about ΔP_i <6 kPa, which may indicate that the spherical modeling is less suitable for low inflating pressures.

3.2.2.2 Continuous force estimation

To further demonstrate the usability of our sensor we tested its response in computing a continuous force profile, during the final steady-state interaction as well as the transient of a palpation task. The purpose of this experiment was to preliminary test the feasibility of this method in real cases.

Methods The same procedure as described previously was used. 12 subsequent making/breaking contact actions with the ATI sensor were carried out: the pneumatic balloon

in its housing was manually pushed toward the ATI, rigidly attached to a flat surface. For each contact action ΔP_i was again the minimum value before the pressure peak (yellow star). Instead, ΔP_f changed continuously: at each instant it corresponded to the current value of internal pressure, as indicated by the red stars in Fig. 3.6c. During this trial, the initial pressure was set to 7.7 kPa.

Results As expected, the results for $(P_f - P_i)$ <0.5 kPa were affected by larger errors. Thus, these values were excluded and the consequent missing part of the force profile was reconstructed by interpolating data obtained for higher ΔP_f with the zero force values before the contact. The middle panel of Fig. 3.6c shows the reconstructed force profile in red and the output of the ATI in blue. To clarify the presentation of results, the delay of the estimated force has been artificially removed introducing a time shift of -0.12 s, computed by aligning the peaks. As shown in the lower panel of Fig. 3.6c, the estimated force trend is similar to the ground truth, with a RMSE of 0.578 N most due to the interpolation done for low forces values.

3.3 Discussion

Results obtained using the pneumatic sensor in peak force estimation were compared to those obtained when applying to the same trials the two methods explained in Section 3.1.1. We evaluated the results obtained applying Lulevich's method to those trials where the assumptions of volume's conservation and small deformations are reasonable, i.e., ΔP_i >8.85 kPa. In this case, the mean normalized error using Lulevich's formula is 14.15%. Applying Shanahan's adjustment (Eq. (3.6)), the error is 14.12%. Under the same conditions, our approach lead to an error of 6.77%. The better performance achieved by our method is due more to the use of Eq. (3.13) to compute R_f than to the small contribution of the gas compression obtained from Eq. (3.11). In fact, stretching is the most contributing to the contact force, compression has negligible values, and the ratio between bending and stretching forces grows with the compliance of the balloon, from around 0.5% to 2%. The small contribution of the bending force was expected due to the results obtained by Lulevich et al. in another paper [113], in which shell bending was considered insignificant.

This comparison allows us to believe our approach is meaningful. Moreover, it can be used to prove that the initial inflating pressure value is fundamental to distinguish contacts leading to small or large deformations. In fact, if we use the variation of volume as the only threshold (e.g., $\Delta V/V_i < 0.2$) to identify which trials are under the assumption of small deformations, mean errors increased to 43.88% for Lulevich's case and 52.27% for

Shanahan's adjustment. It is clear that the assumption of low variation of volume is not sufficient to guarantee small deformations, while high pressure is more likely assuring a spherical shape after contact.

3.4 Conclusions

This chapter explores a model-based approach to estimate contact forces occurring at the slave side during robotic surgery. In this work, we define the relationship between the contact force and the subsequent variation of pressure inside the pneumatic balloon presented in Chapter 2, modeled as an elastic air-filled sphere and treated using linear elasticity theory. The deformation of the membrane due to the contact with the anatomical surface has been modeled as a radius increment and the occurrence of two flattened areas. Internal pressure, displacement due to compression, and radius of the extended sphere were required to compute the reaction force. While the first value is real-time measured, to estimate the deformation and the incremented radius we evaluated the forces acting on the balloon to balance the effect of the contact force, i.e., stretching, bending and compression. Moreover, the ideal gas law was used to take into account the variation of volume due to the contact.

The mathematical model of the deformation was validated through experiments consisting in consecutive contact actions with a commercial force sensor, used as ground truth. The results showed agreement between model predicted and experimental data, with a mean error correspondent to the 9.14% of the real force value in the range [1-3.5] N. In addition to estimating contact force peak values, we demonstrated the feasibility of this method in continuous measurements, proving a high reliability of the system both in the transient and in the steady-state interaction. Other approaches related the interaction force between a spherical object and a rigid surface to the variation of some geometrical parameters, but they were limited to very small deformations and led to larger errors if compared to our method.

Compared to the results of Chapter 2, the model-based approach here presented proves to be more general, accurate, and reliable. The force-pressure relationship is the result of a mathematical model and it is easy to tune against changes of components or design parameters. The only element requiring an experimental detection when size or material change is the balloon radius, but it is far simpler than a complete characterization of the system behavior empirically performed.

All the advantages of the first prototype have been kept. In particular, the resolution and the range of the pneumatic sensor are customizable, depending on the material the membrane is made, the pressure it is inflated at, the balloon size, and the features of the

pressure sensor. However, we are aware of the limitations affecting the present study. The experimental validation we conducted relies only on tests on a rigid surface (the ATI sensor) at the contact. For future development, experiments with softer surfaces will be considered. In addition, our pneumatic sensor is not capable of measuring very small values of force (<1 N) nor giving information about the direction of the applied force.

Future work will involve characterizing the usability of the proposed device while displaying the estimated forces at master side. Feasibility in practical usage will be explored to investigate also if the delay due to the slightly slow dynamics might represent an issue for high quality haptic feedback. The limitations of the sensor in low pressure case will be addressed by exploring different biocompatible elastic materials. Then, future objectives will be the reduction of the prototype size and the actual integration with surgical tools.

3.A Stiffness estimation

A further application of the pneumatic force sensor consists in estimating the compliance of a tissue. In this case, two pneumatic balloons are required. Each balloon is hidden deflated in a tiny hollow inside the instrument and can be controlled separately. When force measurement is required, a single balloon is inflated and comes out of the instrument. When stiffness measurement is required, both the balloons are inflated and come into contact with the tissue.

Considering the tissue at the contact point as a spring, its stiffness can be computed as ratio of force and deformation after the contact. Chapters 2 and 3 explained how to estimate the contact force starting from pressure measurements. Instead, the deformation of the tissue is unknown: from pressure measurements it is possible to known only the deformation of the balloon.

Let's assume it is not possible to correctly measure the deformation of the tissue using vision (e.g., because of occlusions). This issue can be easily overcome by palpating the tissue simultaneously with two balloons of the same size. Defining as F_i the force exerted by each balloon i ($i = 1, 2$), K the stiffness of the tissue, and t_i the deformation of the tissue at each of the two contact points, we can write two equations:

$$F_1 = K * t_1$$

$$F_2 = K * t_2$$

Thus, the stiffness can be computed as

$$K = \frac{F_1 - F_2}{t_1 - t_2}$$

where F_1 and F_2 are known from one of the algorithms proposed in Chapters 2 and 3. Since the two balloons are placed close to each other, we can assume that they touch the tissue approximately in the same area, i.e., there are not significant unevenness among the two contact areas. Thus, from geometrical considerations, if the initial radii R_1 and R_2 are equal, the difference between t_1 and t_2 is equivalent, in modulus, to the difference between the deformations of the two balloons d_1 and d_2, as depicted in Fig. 3.8. The stiffness of the tissue can be computed as

$$K = \frac{F_1 - F_2}{d_2 - d_1} \tag{3.14}$$

where d_1 and d_2 are known from the algorithm proposed in Chapter 3.

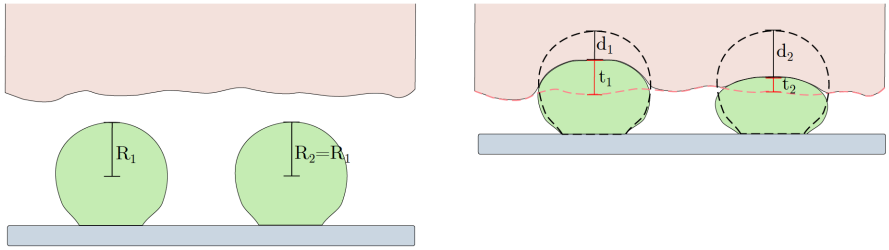

Figure 3.8: On the left, two spheres of the same size coming out from a device. The tissue is depicted in pink. On the right, the two spheres are in contact with the tissue: d_1 and d_2 are the deformations of the two spheres, while t_1 and t_2 are the deformations of the tissue at the two contact points. The red dashed line represents the profile of the undeformed tissue, while the black dashed line represents the profile of the undeformed spheres. Approximately, it can be considered $d_1 + t_1 = d_2 + t_2$.

To perform stiffness measurements, it is important that the two balloons exert different forces $F_1 \neq F_2$ and cause different deformations $t_1 \neq t_2$ on the tissue. For this reason, the two balloons need to be inflated at different pressure values $P_1 \neq P_2$. However, the simple geometrical trick exploited to obtain Eq.(3.14) relies on the equivalence of the initial radii and, under the same conditions (same material and thickness of the membrane, inflating gas, etc.), there is a one-to-one correspondence between inflating pressure and initial radius. Thus, it is not possible to have two identical balloons with the same initial radius but different inflating pressure. To achieve this condition, the two balloons need to be different, e.g., because of materials with different stiffnesses used for the elastic membranes. To guarantee different inflating pressure values, it is necessary that each balloon is connected to a separate pneumatic circuit composed of two solenoid valves, a pressure sensor, and pipes, while air compressor and controller can be shared.

In theory, it would be possible to create a stiffness map by moving the tool along a sequence of predetermined positions on the surface of the organ/tissue and measuring the stiffness in those points.

3.B Vision-based force sensing

A second modality to estimate forces using the pneumatic balloon has been considered for future developments and it is based on the estimation of the deformation of the elastic membrane by means of the cameras already embedded in the surgical system.

Most of the studies on force estimation based on vision techniques reduce the field of application to deformable objects and elastic tissues. For example, the force measurement algorithm presented in [114] uses only data from the contour of deformable and linear elastic objects, generalizing the method to different geometries. In such work, by limiting the study to two-dimensional forces, promising results have been achieved. In the same context of monitoring the deformations of a membrane composed of elastic material, it is possible to develop a new strategy based on the pneumatic balloon.

The membrane of the balloon can be characterized by a plurality of markers to be tracked. Markers are small reference areas or points arranged according to a predetermined pattern, as a regular mesh or matrix. By monitoring the markers it would be possible to estimate the contact area during the palpation procedure and, from the knowledge of pressure value and contact area, the contact force would be estimated. While the previously presented mathematical model allowed us to estimate some geometrical parameters of the balloon starting from pressure measurements, here, on the contrary, the knowledge of the contact area is obtained through vision and is the crucial point of the algorithm.

To estimate the contact area, the camera observes the pneumatic balloon during the whole palpation procedure. At the beginning, the balloon is not in contact with the tissue and the image of the undeformed balloon is recorded. Then, when the balloon comes into contact with the tissue, a number of markers will disappear from the detected image. The number of markers no longer visible is proportional to the contact area. To track the balloon surface a large number of strategies can be exploited. Markers can be lines arranged in a grid or in a particular geometry and can have a distinctive color or thickness depending on the position on the geometrical pattern.

The advantages of this solution is that surgical systems already include cameras and that from this technique it would be possible to determine the orientation of the contact surface and, thus, the direction of the contact force. Also in this case, only passive electronic-free components are introduced into the patient's body and the sensor fully complies with the size restrictions imposed by robotic surgery. However, vision systems can be limited by occlusions due to the interaction between the monitored object and the human body. This reason, together with the complexity of the visual analysis and

the high computational load, made us prefer the fully pneumatic-based method for a first implementation. However, a further extension of this work towards vision-based techniques will be considered.

Chapter 4

A pneumatic sensing cover for hand-held surgical drills

Up to this point, a novel pneumatic device for measuring contact forces during robotic surgery has been investigated. In this chapter, a similar concept has been applied to open surgery, which, in some cases, may suffer from a reduction of tactile perception as well. In fact, despite during open procedures surgeons directly interact with the patient's body, there exist surgical tools, e.g., drills, that limit the haptic capabilities. As already stated in Section 1.3.4, a common issue in surgical drilling is that vibrations generated by the tool prevent the surgeon from clearly perceiving the interaction between the drill and the patient's body. Despite the recent achievements in the development of open surgery tools, preserving the haptic capabilities during drilling tasks is still an open issue.

In this chapter, a novel tool for hand-held drills composed of a cover for force sensing and a haptic display for force feedback is presented. The cover consists in a pneumatic device developed to estimate the contact force occurring during the interaction between drill bit and bones. We propose a pneumatic method to measure the force without modifying the internal structure of the tool, by creating an instrumented cover that can be easily customized and adapted to the off-the-shelf hand-held drills. A performance comparison with a precise commercial force sensor proved the reliability of the measurements. Moreover, the proposed system is capable of rendering the force feedback to the user by means of a haptic display. It consists in a haptic ring in charge of providing cutaneous sensations helping the surgeon in performing the task. The effectiveness of our method has been confirmed by experimental results and supported by statistical analysis.

To the best of our knowledge, this represents the first attempt to assist a surgeon with haptic feedback in open surgery without modifying the existing equipment.

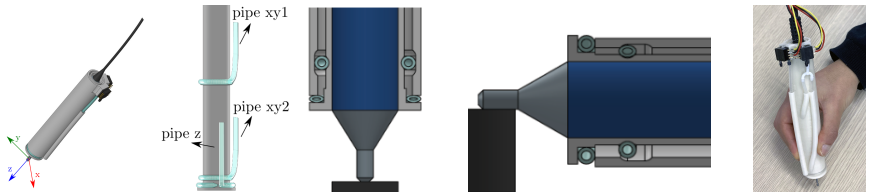

Figure 4.1: The developed sensing system: (a) CAD model; (b) attachment of pipes to the inner shell; (c)(d) details of the sensing mechanism measuring perpendicular and tangential forces, respectively; (e) a user holding a surgical drill enriched with the sensing cover. Outer soft silicone pipes are covered by rigid housings to prevent the surgeon from touching them and affecting the measurements.

4.1 Design of the pneumatic force sensor

4.1.1 Working principle

The main novelty introduced with this work is represented by the sensing part. Measuring contact forces between the drill bit and a surface without modifying the internal structure of existing tools encounters several non-trivial challenges. Because of the drilling task, the sensing system has to be placed far from the contact point. Moreover, a suitable sensor should be reliable, tiny, and lightweight. Unfortunately, common precise and accurate three-axis force sensors are bulky and not suitable for small devices such as surgical drills.

In a first approach to the problem, two different solutions were tested. The former involved two ATI Nano 17 force sensors placed directly on the drill handle to measure interaction forces between the hand and the drill, and therefore reconstruct the force exerted on the bone. This solution was accurate but extremely bulky and uncomfortable for the surgeons. The second solution was based on a similar principle to the one that will be proposed in this chapter (i.e., an instrumented cover), but the sensing elements were force-sensing resistors (FSR400, Interlink Electronics, USA). In this case, we encountered several issues in accurately measuring forces due to the low accuracy and fidelity of the force sensors in the considered application.

For these reasons, we developed a pneumatic system capable of estimating forces using pipes and air pressure sensors, adapting and improving the method introduced in Chapter 2. The great advantage of using a pneumatic system is that it is lightweight, tiny, and measurement information is transferred by means of a gas to the sensors, which can

be located far from the contact point (out of the operational workspace). Also in case of open surgery, placing the electronics outside the human body is an advantage. This approach is beneficial also due to the cost reduction and the use of disposable materials already used in surgery, such as silicone.

The exploited solution is a sensing structure consisting of two concentric cylindrical shells separated by a gap, as shown in Fig. 4.1a. The inner shell (depicted in Fig. 4.1b) is rigidly attached to the body of the drill, while the outer shell is the one held by the surgeon. Soft silicone pipes are placed between the two shells to fill the gap, preventing any relative movements when no forces are applied. They represent also the sensing element of the device, due to the compression generated on the pipes when the drill touches a surface, as explained below.

The working principle of the developed sensing system relies on the assumption that the drill-hand system is under mechanical equilibrium conditions until an external force is applied to the drill bit. When the drill bit comes into contact with the bone, the inner shell moves towards the outer shell (which is held in place by the surgeon's hand) along the direction of the contact (see Figs. 4.1c and 4.1d). This displacement generates a compression of soft silicone pipes depending on the external force. Thus, the device acts as a spring-mass system, which is under equilibrium conditions until the external force induces a compression of the spring, i.e., the pipes. Such a compression can be estimated using air pressure sensors, which measure the increase of pressure into the pipes and can be advantageously placed outside the outer shell.

In this device, the location of the soft silicone pipes is of the utmost importance. For example, a pipe placed on a flange of the inner shell is capable of detecting forces along the vertical axis of the drill (as in Fig. 4.1c), while it is not compressed when the drill is parallel to the contact surface (as in Fig. 4.1d).

In the considered surgical scenarios, torque components are treated as negligible, because the drill bit does not enter deeply into the bone generating significant values of torque. It is worth noting also that the grasp squeezing forces applied by the surgeon do not cause any structural deformation of the pipes thanks to the high stiffness of the external shell. Then, the only deformations are due to the forces applied to the drill bit.

4.1.2 Hardware implementation

As depicted in Fig. 4.1e, we present a proof of concept in which the pneumatic force sensor is composed of two 3D-printed parts made of ABSPlus (Stratasys Inc., USA), soft silicone pipes (ID 2.5 mm, OD 3.5 mm), and two 2 kPa differential pressure sensors (MPXV7002DP, NXP Semiconductors, NL) measuring forces along the z-axis and on the xy-plane, respectively. The reference system is depicted in Fig. 4.1a. The total weight

of the cover is 51 g. Differently from the pneumatic balloon presented in the previous chapters, pipes are not additionally inflated: at the steady state they are at the equilibrium with the external air pressure. Since air into the pipes is not pressurized, this device does not need external equipment to supply air.

Each pipe is ring-shaped and firmly attached to the inner shell as shown in Fig. 4.1b, with one end leak-proof sealed and the other one connected to the pressure sensor. In particular, forces on the xy-plane are measured by a sensor connected to *pipes xy*. In this case, two pipes spaced along the length of the drill are required to prevent possible relative movements between the two shells when no forces are applied. It is worth pointing out that in this configuration it is not possible to decouple forces along x-axis and forces along y-axis. Thus, the use of two pipes does not aim at separately measuring the two components but has the only purpose of avoiding backlash. Since *pipes xy* measure forces on the same plane, they are jointed together and connected to a single pressure sensor. It is important to notice that each of the two pipes goes out of the outer shell as soon as the loop close, through a small hole. In this way, there is no overlapping of pipe between the two shells, which means that the sensing component has the same size in each point and, thus, the measurement resolution is the same in all the directions of the xy-plane.

Both the shells contain grooves for enclosing the pipes so as to reduce the width of the device. The result is that the gap between the shells corresponds to the internal diameter of the pipes. In the outer shell, the cavity is vertically extended so as not to detect pressure variations in *pipes xy* when the only force involved is along the z-axis (i.e. when the outer shell just slides over the inner shell).

Forces along the z-axis are supposed to be detected only by a third pipe, i.e., *pipez* (see Fig. 4.1b and Fig. 4.1c), taking advantage of the flange on the lower part of the shell. When the drill is vertically pushed towards a surface, the pipe placed on the flange will be pressed by the outer shell, and a second pressure sensor will measure such a pressure variation.

The final force estimation will be the norm of the force along the z-axis and the force on the xy-plane. Depending on the orientation of the drill, the contribution of each of these two force components may change. However, since the final force estimation is the norm of these components, the orientation of the drill does not influence the final value.

It is worth noticing that a pipe is less sensitive in close proximity of the point in which the ring is closed, defined as “closure point”. This is not relevant in case of *pipe z*, because during measurements on the z-axis the entire length of the ring is always involved, and, thus, even if the “closure points” cannot be properly squeezed by the outer shell, the remaining part of the pipe can compensate for it. For what concerns the xy-plane, this is not true as well. In this case, during the contact between the drill bit and a surface

only a portion of the ring is squeezed, depending on the direction of the force and the inclination of the drill. If the involved portion of *pipes xy* corresponds to the "closure points" of the rings, the quality of the estimation may be affected. Thus, the "closure points" of *pipe xy1* and *pipe xy2* were both placed on the bottom side of the drill handle. In this way, measurements carried out by these points correspond to forces exerted by the drill from bottom to top, which never occur in surgery tasks.

The effect of gravitational force has been considered negligible with respect to the forces at work, due to the lightweight of the drill. Moreover, we supposed that in a such accurate task the surgeon compensates the weight by his hands and the contact force is equivalent to the force exerted by the surgeon.

For what concerns the hardware solutions, vibrations generated by the drill are filtered by means of a hardware R-C filter with an experimentally selected cut-off frequency of 144.68 Hz. The cut-off frequency of the R-C filter was selected in a preliminary phase, after some ad-hoc designed tests, to reduce as much as possible noises generated at the rotation speed of the drill (i.e., 15.000 rpm). This hardware filter aims at removing the noise in the output of the pressure sensors. To further isolate sensors from vibrations, two tiny sponge layers are placed under the sensor housings. The inserted sponge layers are thin and lightweight: the thickness is 3 mm and the weight is not measurable with the scale. The principal objective of this ploy is to reduce errors in measurements at the sensor level due to the vibrations of the whole drill, regardless the rotation speed.

Analog data from the sensors are acquired using a NI USB-6218 DAQ (NI, USA). Finally, a software algorithm, described below, processes the signal.

4.1.3 Software implementation

A calibration procedure was required to correctly transform data from pressure sensors into forces. The initial calibration was performed with the drill switched off. A high precision ATI Gamma F/T sensor (ATI Industrial Automation, USA) was used to identify the force-pressure relation.

A separate procedure is required for calibrating the two sensors. For what concerns the z-axis calibration, the drill was vertically pushed toward the ATI sensor (covered by a piece of plywood to avoid damages) for a total of 50 contact actions, so that the generated force deforms only *pipe z*, as depicted in Fig. 4.1c. In accordance with the results presented in Chapter 2, data gathered from the pressure sensor and the ATI were quadratically interpolated using a MATLAB© algorithm. The same procedure was repeated for the xy-plane, keeping the drill horizontally (as in Fig. 4.1d). For the tool exploited in this work, the two found relations are: $F_z = 5034 \cdot P_z - 2280 \cdot P_z^2$ and $F_{xy} = 9542 \cdot P_{xy} - 1017 \cdot P_{xy}^2$, being P_{xy} and P_z the pressure values. Once the force-

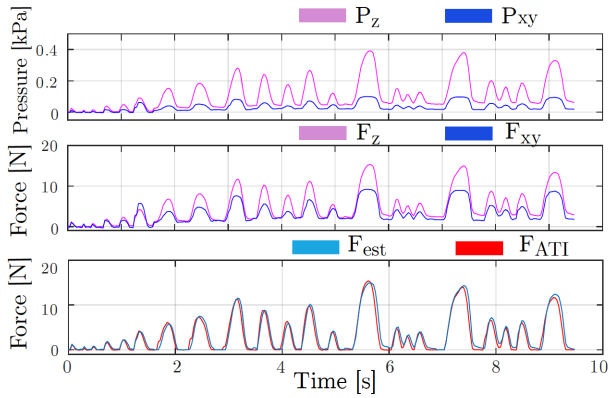

Figure 4.2: Force estimation in case of switched off drill: raw pressure values from the two pressure sensors (upper panel), the correspondent values of force computed using the quadratic relations experimentally identified (middle panel), and the comparison between the final force estimation and the ground-truth value (lower panel).

pressure relations for the z-axis and the xy-plane have been identified, for each pressure value measured by one of the two sensors it is possible to estimate the correspondent force F_z or F_{xy}.

As a final step toward the contact force estimation, the norm of F_z and F_{xy} is computed. Indeed, from the user point of view, there is no need to distinguish the three components of the force: the surgeon just needs to have a feedback on the total force exerted, which corresponds to the norm of F_z and F_{xy}. It is worth pointing out that the projection of the exerted force in the reference system of the drill (i.e., splitting the force in F_z and F_{xy}) has the only purpose of easily measuring its value. In other words, splitting the force in F_z and F_{xy} allows us to estimate the exerted force by means of the proposed pneumatic system, but it is not meaningful from the user's point of view, because, to facilitate the drilling task, it is sufficient for the surgeon to have a feedback on the force exerted along the contact direction, without discerning its three components in any reference system. In this sense, no loss of informative content occurs if the force provided to the user is the norm of the forces computed in the reference system of the drill. As already mentioned in Section 4.1.2, the value of the norm does not depend on the inclination of the drill.

Steps from pressure raw data toward force values are depicted in Fig. 4.2. As noticeable in the upper and middle panels, the value of the force estimation is affected by the relatively slow dynamic of the pneumatic system. After breaking contact, the pressure of the pipes does not immediately reach the initial zero-value. A rapid decrease

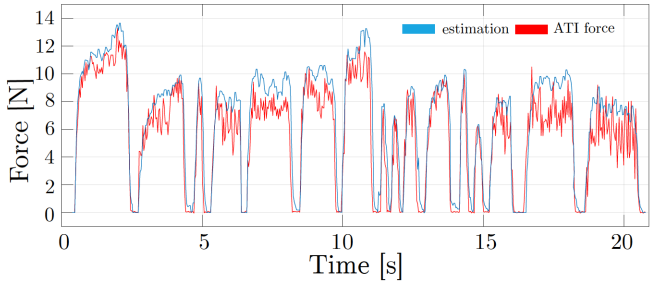

Figure 4.3: Force estimation performed by the pneumatic sensing cover (blue) and ground-truth value (red) in a representative trial affected by vibrational noise.

of the pressure is followed by a slow downwelling. Thus, we introduced a compensation algorithm which brings to zero the *"non-contact offset"*, identified as a flat trend after a significant negative slope.

We validated this method comparing the estimated contact force F_{est} to the norm of the forces measured by the ATI in 200 contact actions involving both the z-axis and the xy-plane. Also in this case, the drill was switched off. The resulting RMSE is 0.967 N, in a force range of [0–18] N. In the lower panel of Fig. 4.2, the comparison with the ATI force value is shown.

Once validated the sensing device in non-vibrating trials, we tested the proposed system switching on the drill. Adding vibrations introduces a significant modification in the force profile, as depicted in Fig. 4.3, thus, to compensate this negative effect, also a software filter has been implemented. The filtered force value corresponds to the maximum value in a moving window of 33 ms. In this way, the downward peaks are ignored guaranteeing a safer overestimation of the force exerted on the bones. Overestimating the force is considered to be the best approach given the particular context (i.e., surgical procedures). However, this implies that it is not possible to numerically compare the filtered force estimation with the measurements of the ATI in drilling tasks, because the force profiles would be quite different. The filtered force is a sort of envelope of the non-filtered signal, thus the point-to-point error would be very large. Despite this, Fig. 4.3 shows that the reconstructed force profile is similar to the one registered by the ATI sensor. The duration of the moving window was selected after numerous preliminary tests, to obtain the best compromise between filter performance and response delay. This filter, in fact, introduces a delay depending on the duration of the moving window, as it is possible to see from the zoomed image depicted in the scheme of Fig. 4.4. This figure shows all the steps of the force estimation. As for non-vibrating trials, the last step of the

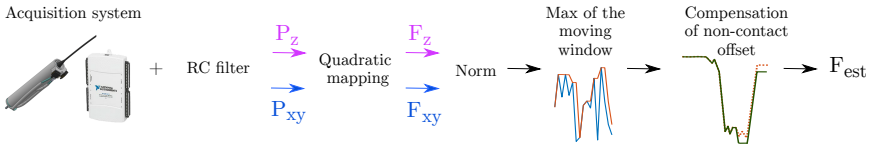

Figure 4.4: Main steps of the force estimation.

force estimation is the compensation of non-contact offset previously explained.

For the sake of clarity, it is worth pointing out that three different approaches have been used to filter the data in order to obtain the best result. In addition to the sponge layer and the RC filter, the software filter intends to refine the estimation and correctly reconstruct the force profile. This procedure can not be done by simply adjusting the cut-off frequency of the hardware filter, because the force profile would be too smooth or too noisy.

4.2 Haptic feedback

Contextually with the force sensing system, we developed a haptic ring capable of generating cutaneous and vibrotactile feedback. The proximal phalanx was demonstrated to be a suitable location for delivering cutaneous and vibrotactile feedback [115, 116, 117]. In the context of this thesis, this was the first attempt to test the performance of one of the proposed sensing devices in combination with a haptic display. To have a lightweight device with a limited encumbrance, we employed a single servo-motor (HS-35HD Ultra Nano, HITEC Inc., USA) controlling a flexible belt for generating cutaneous stimuli and an eccentric-mass motor (EMM)(Precision Microdrives, UK) to generate vibrotactile stimuli [118]. The device is controlled by the same DAQ board used for sensors data acquisition through an ad-hoc library.

The servo motor generates the rotation of a master gear that moves a slave gear. Such mechanism results in opposite spinning directions of the gears, that translate the belt along the vertical axis. The workings are depicted in Figs. 4.5a and 4.5b. The maximum range of the belt motion in the vertical direction is 23 mm and it depends on the external diameter of the gears (11 mm), the length of the belt (95 mm), and the maximum rotation range of the servo motor (120°). We selected these values considering that also fingertips bigger than the average should fit. The maximum exploitable displacement range for force generation is 6 mm, so that the device can apply a maximum force of 3 N considering a stiffness of 0.5 N/m as elastic behavior of the finger pulp. Interested readers